

Bismuth-Integrated Nitrogen-Doped Carbon Nanostructures Enabling Broad Electrolyte Compatibility for Mg-Ion Batteries

Woo Joo No, Jonghyun Han, Mingony Kim, Jihwan Choi, Kyung Yoon Chung, Kwan-Young Lee, and Si Hyoung Oh*

Bismuth has emerged as a promising alloying anode for magnesium-ion batteries (MIBs), offering high theoretical capacity with a low electrode potential, and thus serving as a viable alternative to Mg metal. Herein, Bi nanoparticle (NP)-integrated nitrogen-doped carbon nanostructures (Bi@nCN) are synthesized via a scalable one-step carbothermal reduction of BiOCl and Mg phthalocyanine. The resulting Bi@nCN features finely dispersed Bi NPs embedded in a nitrogen-doped carbon matrix, forming a stress-relieving architecture that accommodates the structural changes associated with the two-phase reaction between Bi and Mg₃Bi₂. Bi@nCN demonstrates excellent electrochemical

performance, with high capacity retention, superior rate capability, and minimal polarization growth. Furthermore, full cells employing Bi@nCN anodes exhibit stable operation in chloride-free electrolytes, including ether- and nitrile-based systems, in which Mg metal typically develops insulating passivation layers. These findings highlight the potential of Bi@nCN to enable stable Mg-ion storage in chloride-free electrolytes, overcoming the intrinsic limitations of Mg metal anodes and expanding the scope of MIB chemistry with new electrolyte and cathode combinations.

1. Introduction

Magnesium-ion batteries (MIBs) have recently garnered substantial attention as promising alternatives to lithium-ion batteries owing to pronounced advantages in terms of material cost and achievable energy density.^[1,2] These features stem from the abundance of Mg resources in the earth's crust (2.33%), almost comparable to Na, and from its low electrode potential (-2.34 V vs SHE), high volumetric capacity (3833 mAh cm^{-3} for Mg vs 2062 mAh cm^{-3} for Li), and low tendency to form dendrites upon repeated plating/stripping of Mg metal.^[3–5] These characteristics make MIBs highly attractive for the next-generation energy storage systems, particularly in large-scale applications

where both safety and cost-effectiveness are critical considerations.^[6,7] Despite these advantages, several technical challenges still hinder the widespread use of magnesium metal anodes, primarily due to the prompt formation of a passivation film on the Mg surface.^[8–10] This ion-insulating layer is spontaneously formed from the reaction of Mg metal with trace amounts of oxygen or residual moisture in the electrolyte,^[11,12] which critically interferes with Mg²⁺ ion transport and retards reversible Mg plating and stripping. Consequently, Mg metal anodes often suffer from poor electrochemical kinetics and low Coulombic efficiency, rendering them unsuitable for practical applications. In spite of recent remarkable progress in the functional electrolytes based on combinations of Lewis acids and Lewis bases in ethereal solutions to address these issues,^[13,14] they have often exhibited undesirable traits as well such as extreme moisture sensitivity, strong corrosivity, high volatility, and insufficient electrochemical stability windows. Consequently, these electrolytes are often incompatible with typical oxide-based cathode materials that are prone to corrosion by active halide species, in spite of their immense potential for achieving higher electrode potential and greater energy density. Therefore, the development of effective strategies to overcome these technical challenges of Mg metal remains an important step toward realizing the practical application of MIBs.

One promising strategy is to replace Mg metal anodes with Mg-alloying hosts that may exhibit better stability in conventional-type electrolyte systems consisting of well-defined salts and solvents and containing no active halide species.^[15] Until recently, various alloying materials such as Bi, Sn, Sb, and Ge have been explored.^[16–19] Among them, bismuth (Bi), based on the formation of Mg₃Bi₂, has emerged among convincing contenders in the light of its high theoretical volumetric capacity ($\approx 3,800\text{ mAh cm}^{-3}$), electrochemical reversibility, and reduced

W. J. No, J. Han, M. Kim, J. Choi, K. Y. Chung, S. H. Oh
Energy Storage Research Center
Korea Institute of Science and Technology
Hwarang-ro 14-gil 5, Seoul, Seongbuk-gu 02792, Republic of Korea
E-mail: sho74@kist.re.kr

W. J. No, K.-Y. Lee
Department of Chemical and Biological Engineering
Korea University
145, Anam-ro, Seoul, Seongbuk-gu 02841, Republic of Korea

M. Kim, K. Y. Chung, S. H. Oh
Division of Energy & Environment Technology
KIST School

Korea Institute of Science and Technology
Hwarang-ro 14-gil 5, Seoul, Seongbuk-gu 02792, Republic of Korea

 Supporting information for this article is available on the WWW under <https://doi.org/10.1002/batt.202500616>

 © 2025 The Author(s). *Batteries & Supercaps* published by Wiley-VCH GmbH. This is an open access article under the terms of the Creative Commons Attribution License, which permits use, distribution and reproduction in any medium, provided the original work is properly cited.

passivation layer formation owing to lowered reactivity with electrolytes compared to Mg metal.^[20,21] Figure S1, Supporting Information, demonstrates that Mg₃Bi₂ can work with electrolyte solvents such as dimethylformamide, which was known to be incompatible with Mg metal. This versatility provides many new opportunities for configuring novel Mg-ion chemistries with higher electrochemical performance. Moreover, Bi was reported to exhibit superior Mg²⁺ diffusion kinetics compared to other alloying-type materials,^[22] facilitating facile insertion and extraction of Mg²⁺ during electrochemical cycling. In addition, the electrode potential of Mg₃Bi₂ formation (≈ 0.23 V vs Mg²⁺/Mg) is only slightly higher than that of pure Mg metal, which contributes to maintaining the overall energy density and efficiency of Mg metal batteries. These features make Bi-based alloys highly promising candidates for next-generation anode materials in MIBs.

Despite the aforementioned advantages, Bi-based anodes currently face some significant technical challenges that impede their practical implementation in MIBs. A primary issue is insufficient Mg²⁺ ion transport at high charge–discharge current rates. The strong electrostatic interactions between Mg²⁺ and the Bi host slow solid-state diffusion, resulting in the limited capacity and shortened cycle life during prolonged cell operation.^[23,24] Furthermore, the large volume changes ($\approx 100\%$) during the alloying/dealloying process lead to gradual pulverization of electrode active materials and instability in electrical contact over extended cycling. Various strategies have been explored to mitigate these issues, such as reducing particle size to the Nanometer scale through nanoparticle (NP) synthesis or the preparation of porous structures using diverse methods.^[16,21,25,26] For example, monodisperse Bi nanocrystals have been obtained via low-temperature colloidal or polyol synthesis;^[21,25] Bi nanotubes have been hydrothermally grown;^[16] and porous Bi has been prepared by chemical leaching of Sn–Bi alloys.^[26] These approaches effectively relieve stresses and strains caused by large volumetric changes, but they often suffer from limited scalability and low tap density. In other efforts, Bi NPs were embedded into a conductive carbon matrix to buffer volume expansion while simultaneously enhancing both electronic and ionic accessibility to the redox sites.^[27–29] However, challenges such as inhomogeneous Bi particle distribution, facile agglomeration, and structural instability continue to limit overall electrochemical performance. Additionally, multielemental alloy systems, such as Mg–Bi–Sn and Mg–Bi–Sb, have been investigated to improve reaction kinetics and structural stability.^[30–32] While these strategies aim to enhance both kinetics and electrochemical stability, they often involve increased synthetic complexity and pose difficulties for large-scale implementation. Moreover, the full mechanistic understanding of how alloying elements contribute to performance enhancement remains incomplete. Therefore, although Bi–Mg alloys hold great promise as potential anode materials for MIBs, substantial research efforts are still required to overcome these critical limitations and fully realize their potential.

In this work, Bi NP-integrated nitrogen-doped carbon nanostructures (Bi@nCN) are proposed as a viable anode material with wide electrolyte compatibility for MIBs. Bi@nCN was synthesized

via simple CVD-like process using BiOCl and magnesium phthalocyanine (Mg-Pc) as precursors. In Bi@nCN, Bi NPs were finely dispersed in a nitrogen-doped carbon matrix derived from thermal decomposition of Mg-Pc. This nanostructure enhanced Mg²⁺ ion diffusion kinetics and served as an effective buffer to accommodate volume expansion during the alloying–dealloying process. As a result, the Bi@nCN electrode exhibited excellent rate capability and cycling stability. Moreover, Bi@nCN was demonstrated to function in those electrolyte environments that are incompatible with Mg metal,^[33,34] paving a new way to develop advanced MIBs.

2. Results and Discussion

2.1. Synthesis and Structural Characterization of Bi@nCN

Bi@nCN was prepared by a one-step carbothermal reduction process employing BiOCl NPs and commercially available Mg-Pc at a temperature of 700–900 °C, as illustrated in Figure 1a. This approach is much simpler and more scalable compared to conventional multistep methods for preparing similar functional composites.^[16,21,25,26] BiOCl nanoplatelets were prepared via controlled hydrolysis of BiCl₃ (Figure S2, Supporting Information). MgPc retains plenty of Mg–N₄ moieties in the structure, which can be transformed into the N-doped carbonaceous material via a CVD-like process at elevated temperature.^[35] During the thermal process, the decomposed carbon precursors were vaporized to wrap BiOCl particles, forming Bi NPs gradually via carbothermal reduction. In this work, MgPc was selected over other M-Pc's because for such materials as Fe-Pc and Ni-Pc, the resulting carbon would contain a significant amount of doped heavy metal species that could be detrimental to the electrochemical performance. To find out the optimal synthetic conditions, thermogravimetric analysis (TGA) was conducted to examine the thermal decomposition behavior of the individual and mixed precursors. As depicted in Figure 1b, pristine Mg-Pc exhibited a sharp weight loss at around 450 °C in the inert atmosphere to initiate the carbonization to form a nitrogen-doped carbon matrix. BiOCl displayed thermal stability up to higher temperatures, with a minor weight loss observed near 800 °C, due to BiOCl decomposition and partial Cl evaporation.^[36,37] For the mixture of BiOCl and Mg-Pc, significant weight loss was observed at around 600 °C, indicative of the onset of carbonization of Mg-Pc, while the gradual weight decrease afterward represented the carbothermal reduction of Bi³⁺ to metallic Bi⁰. This enabled finely dispersed Bi NPs in the nitrogen-doped carbon matrix of Bi@nCN. The formation of Bi metal in the carbon matrix was confirmed by X-ray diffraction (XRD) measurements, as described in Figure 1c. The diffraction peaks of the Bi@nCN annealed at 700 and 900 °C (denoted as Bi@nCN-700 and Bi@nCN-900, respectively) were consistent with those of Bi metal with a trigonal space group, R $\bar{3}m$ without any impurity phase. The average crystallite size of Bi NPs was estimated from the strongest (102) reflection using the Scherrer equation, yielding ≈ 59 nm for

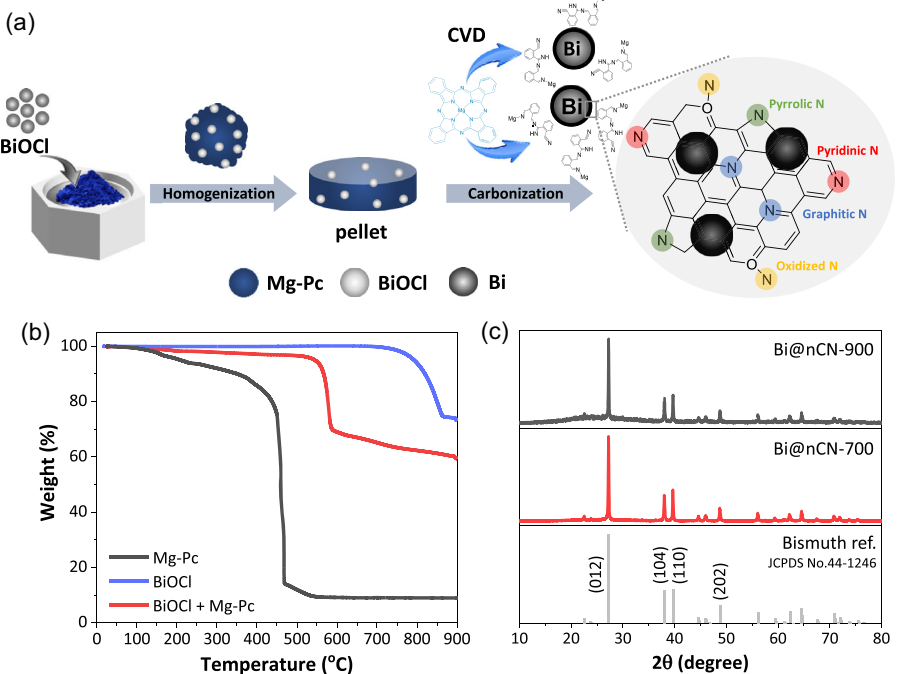


Figure 1. a) The schematic illustration of the synthetic process for Bi@nCN. b) TGA results of Mg-Pc (black), BiOCl (blue), and mixed precursors (red) indicative of thermal decomposition in Ar atmosphere. c) XRD patterns of Bi@nCN synthesized at 700 and 900 °C.

Bi@nCN-900 and 48 nm for Bi@nCN-700,^[38] showing \approx 23% grain growth at the higher synthetic temperature. Since larger crystallite size for Bi metal may involve more intense accumulation of stresses and strains during electrochemical alloying cycling, excessive growth should be suppressed as much as possible to enhance the electrochemical performance of Bi@nCN.^[39]

The local structural features of Bi@nCN composites were probed through Raman spectra, which were utilized to evaluate the degree of graphitization and associated structural disorders in the carbon matrix. As shown in Figure 2a, all Bi@nCN composites exhibited distinct D and G bands centered at \approx 1360 and

1580 cm⁻¹, corresponding to disordered and graphitic carbon structures, respectively.^[40] The areal intensity ratio (I_D/I_G) was calculated to evaluate the defect level, yielding similarly large values, 3.41 for Bi@nCN-700 and 3.21 for Bi@nCN-900. These values are substantially larger compared to those observed in the carbons prepared from Fe-Pc or Ni-Pc, where catalytic graphitization occurred in the corresponding temperature ranges.^[41,42] Moreover, similar I_D/I_G ratio for both Bi@nCNs indicated that electrical conductivity might not be significantly benefited by higher synthetic temperature for Mg-Pc. In contrast, the relatively low I_D/I_G values observed for Bi@nCN materials in general suggested a greater

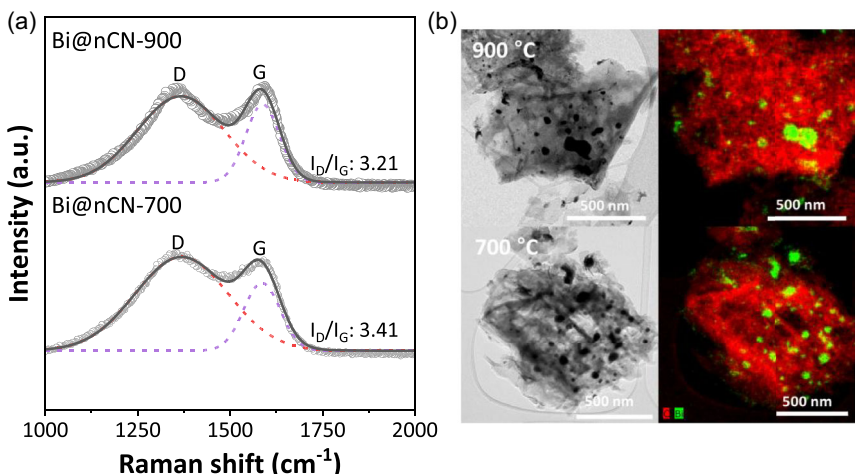


Figure 2. a) Raman spectra and b) HR-TEM images and corresponding energy-dispersive spectroscopy mapping of Bi@nCN particles synthesized at 700 and 900 °C.

density of structural defects in the carbon framework that might provide more anchoring sites for Mg^{2+} adsorption and desolvation, thereby facilitating surface transport to redox sites in Bi NPs.^[27,43] Then, the dispersion and uniformity of Bi NPs in the carbon matrix were evaluated using high-resolution transmission electron microscopy (HR-TEM). As shown in Figure 2b, Bi@nCN-900 exhibited larger and more agglomerated particles due to the high synthesis temperature, where Bi NPs could coalesce owing to the low melting point of Bi metal (271.5 °C). In contrast, Bi@nCN-700 appeared less agglomerated (Figure S3, Supporting Information) with a moderate size distribution centered around 40 nm (Figure S4, Supporting Information) ($D_{50} = 36.8$ nm). These features are considered favorable for improving cycling stability, as they would trigger less dislocation formation and pulverization from the intense volume change during repeated alloying–dealloying.^[26,44,45]

X-ray photoelectron spectroscopy (XPS) was performed to look into the chemical states of the carbon matrices and Bi NPs in Bi@nCN prepared in different synthetic temperatures. The C 1s spectra (Figure 3a,b) indicated that slightly more sp^3

(284.5 eV) carbon was observed in Bi@nCN-900, consistent with the results from Raman analyses, where Bi@nCN-900 exhibited a slightly lower I_D/I_G ratio with a more graphene-like structure. A similar trend was also observed in the N 1s spectra (≈ 400 eV, Figure 3c,d), which were deconvoluted into pyridinic (≈ 398 eV, N_{PD}), pyrrolic (≈ 399 eV, N_{PL}), graphitic (≈ 401 eV, N_{GP}), and oxidized (≈ 404 eV, N_{OX}) components,^[46–49] as described in Figure 1a. Bi@nCN-900 exhibited a larger fraction of graphitic moieties, with relative ratios of $N_{PD} : N_{PL} : N_{GP} : N_{OX} = 17:22:46:15$. These findings suggested that Bi@nCN-900 might have slightly higher degree of graphitization and thus higher electronic conductivity compared to Bi@nCN-700, which was confirmed by conductivity measurement (Figure S5, Supporting Information). However, as discussed based on the Raman spectra, the structural difference did not appear to be substantial enough to have a significant impact on the electrochemical performance. Meanwhile, for Bi@nCN-700, the pyridinic component in the doped nitrogen was predominant ($N_{PD} : N_{PL} : N_{GP} : N_{OX} = 37:23:23:17$), and the overall nitrogen content decreased substantially from 9.61% to 1.68% as the synthesis temperature increased from 700 to 900 °C, likely

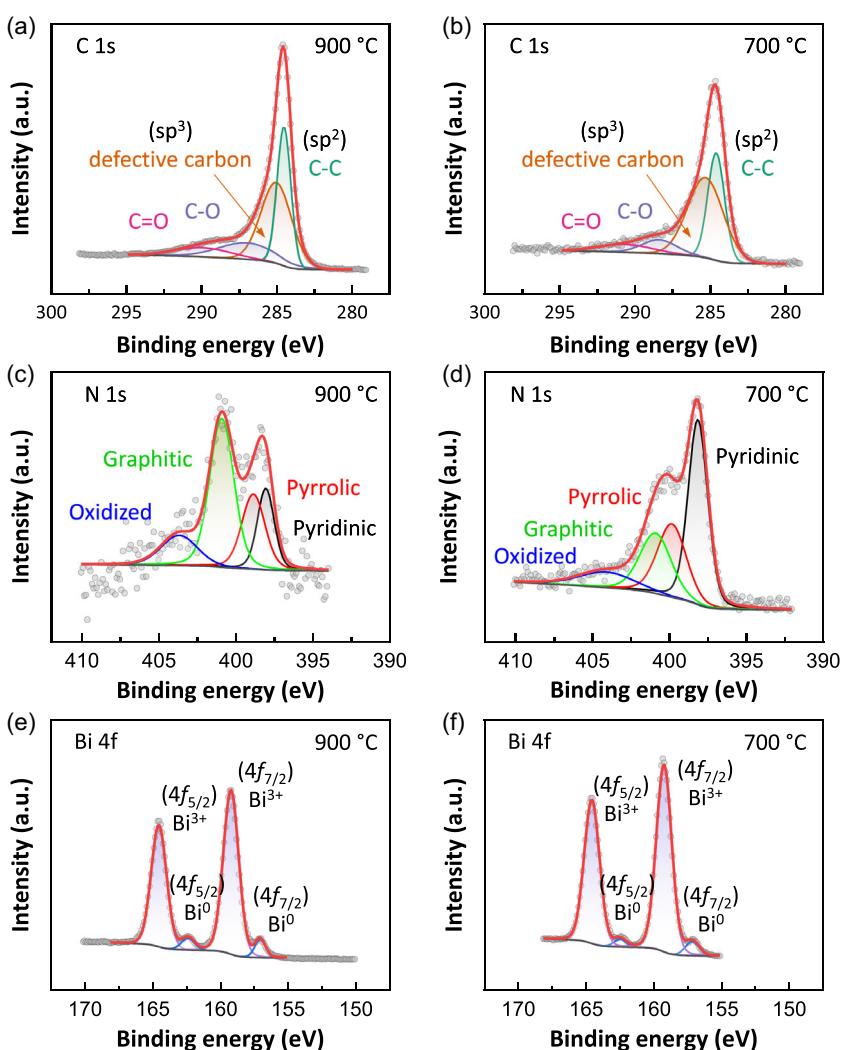


Figure 3. XPS analysis of the Bi@nCN-900 and Bi@nCN-700. a,b) C 1s, c,d) N 1s, and e,f) Bi 4f spectra of Bi@nCN-900 and Bi@nCN-700, respectively.

due to thermal evaporation of nitrogen atoms (Figure S6, Supporting Information).^[49–51] Consequently, the density of pyridinic-N—which can coordinate with Mg²⁺ ions^[46] and provide anchoring sites beneficial for the alloying reaction with Bi—is considered to be significantly higher in Bi@nCN-700. The chemical state of Bi was observed with Bi 4f spectra (Figure 3e,f), where metallic Bi component was confirmed by the Bi⁰ peak ($4f_{7/2}$, 157.1 eV). The observation of Bi³⁺ peak ($4f_{7/2}$, 159.2 eV) was likely caused by the reoxidized surface upon exposure to air, indicating that the surface is covered with thin Bi₂O₃ layer.^[28] Since electrochemical behavior depends on a blend of these factors, these chemical and structural factors should be considered for the best performance.

2.2. Electrochemical Performance and Mechanistic Studies of Bi@nCN

To evaluate the basic electrochemical performance of Bi@nCNs, coin cells were manufactured using Mg metal as a reference

electrode and all-phenyl-complex (APC)^[14] as an electrolyte system, and galvanostatic charge–discharge measurements were conducted at various current rates. As shown in Figure 4a, the voltage profiles at 0.1 C ($1\text{C} = 385 \text{ mA g}^{-1}$) exhibited well-defined plateaus around 0.3 and 0.25 V during the discharge and charge processes, respectively. These plateaus corresponded to the alloying / dealloying reaction between Bi and Mg²⁺ to form Mg₃Bi₂, indicative of a two-phase reaction between Bi and Mg₃Bi₂.^[52] The relatively small associated overpotential, together with a nearly theoretical delivered capacity, indicates the highly reversible nature of the alloying reaction enabled by the nanocomposite strategy employed in this work. The initial irreversible capacity might be attributed to the conversion of residual BiOCl or surface Bi₂O₃ to metallic Bi, which disappeared in subsequent cycles.^[25] It is noteworthy that this irreversible capacity was observed to be much larger when Fe-Pc was used instead of Mg-Pc, where the doped Fe in those carbons likely acted as an irreversible redox center (Figure S7, Supporting Information). Moreover, the much smaller reversible capacity in the case of

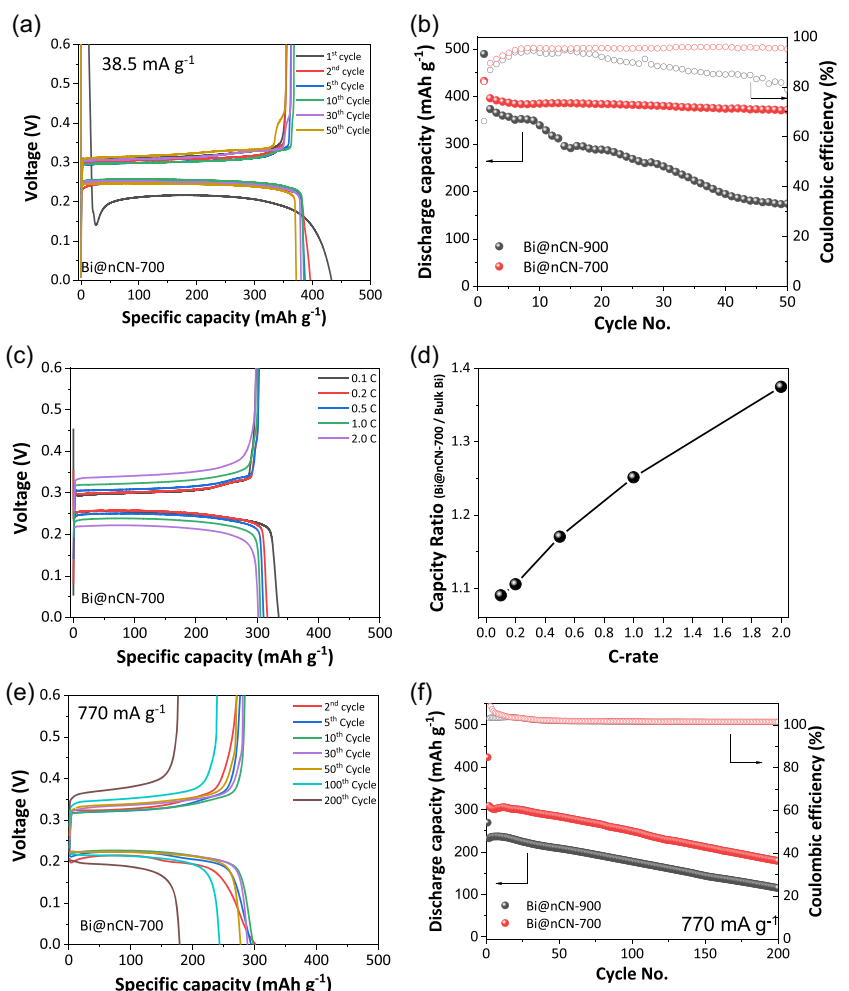


Figure 4. Electrochemical characterization of Bi@nCN electrode. a) Galvanostatic discharge–charge profiles of Bi@nCN-700 electrode at 0.1 C. b) Cycling performance of Bi@nCN-700 and Bi@nCN-900 electrode at 0.1 C. c) Rate capability of Bi@nCN-700 at various C-rates (0.1–2.0 C). d) Discharge capacity ratio of Bi@nCN-700 to Bulk Bi electrode (Bi@C-BM) at various C-rates (0.1–2.0 C). e) Discharge–charge profiles of Bi@nCN-700 at 2.0 C for an extended duration of over 200 cycles. f) Cycling performance of Bi@nCN-700 and Bi@nCN-900 electrodes at 2.0 C for 200 cycles. All electrochemical tests were performed in a half-cell configuration with APC electrolyte.

Fe-Pc was ascribed to the significant amount of heavy metal doping in the carbon matrix. Therefore, the selection of Mg-Pc among various M-Pc candidates is crucial in this study, given that Mg has a low atomic weight and does not serve as a redox-active center for Mg^{2+} . As shown in Figure 4b, the cell containing Bi@nCN-700 exhibited remarkable capacity retention, preserving about 94% of its initial capacity over 50 cycles, and maintained good Coulombic efficiency (CE) throughout the cycling, as opposed to that with Bi@nCN-900 (Figure S8, Supporting Information). This is likely attributed to the smaller size and less agglomerated architecture of Bi@nCN-700, which could be more effective in mitigating stress induced by volume changes during cycling. After stabilization, the ultimate CE for Bi@nCN-700 approached 96.3%, indicating that the formed SEI on Bi metal may not be completely durable upon the large volume change during the alloying process,^[26,45] suggesting that further refinement is required in future work. In addition, the rate capability of Bi@nCN-700 was evaluated at various current densities ranging from 0.1 to 2.0 C, as shown in Figure 4c. The Bi@nCN-700 electrode retained a distinct voltage plateau up to 2.0 C, maintaining \approx 90% of capacity at 0.1 C as opposed to 71% for bulk Bi particles prepared by simple ball milling (Figure S9, Supporting Information). The increasing capacity ratio with current rate in Figure 4d implies that the Bi@nCN structure provided faster Mg^{2+} transport and preserved its integrity

better under high current rates compared to bulk Bi. The long-term cycling performance of Bi@nCN was investigated at 2.0 C. Bi@nCN-700 maintained its initial voltage profiles well up to 100 cycles (Figure 4e), and delivered much higher reversible capacity (179 vs 115 mAh g⁻¹) and capacity retention (58 vs 49%) after 200 cycles compared to Bi@nCN-900 (Figure 4f). This might indicate that larger number of structural defects in the carbon matrix in Bi@nCN-700 facilitated quicker surface transport of Mg^{2+} to redox sites as previously discussed. These results verified that the Bi@nCN-700 sustained good reaction kinetics and structural stability even under prolonged high-rate cycling. Despite its simple synthetic route, it exhibits competitive electrochemical performance compared with previous studies that employed nanocomposite or alloying strategies (Table S1, Supporting Information).

To confirm the two-phase reaction mechanism, *in situ* XRD patterns were collected continuously during the discharge-charge process of the initial two cycles, which showed the real-time formation of Mg_3Bi_2 through the alloying reaction between Bi and Mg^{2+} (Figure 5a). The peak near 43° corresponded to the Cu current collector of the working electrode, while the peaks around 32° and 36.5° were identified as those from Mg metal in the counter electrode. These reference peaks remained constant throughout the discharge and charge, serving

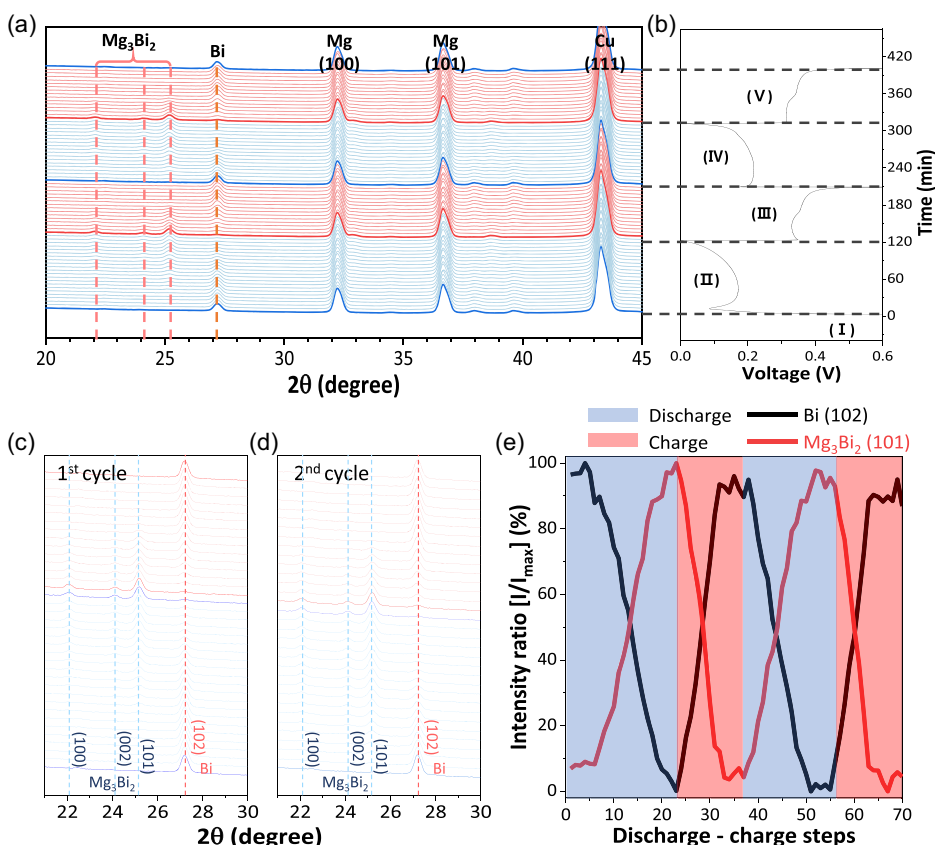


Figure 5. a) Evolution of *in situ* XRD patterns for Bi@nCN-700 anode during galvanostatic cycling for two cycles at 0.5 C. b) The associated voltage–time profile with five regions (I–V) indicated. c,d) Enlarged view of *in situ* XRD patterns in first cycle and second cycle, focused on Mg_3Bi_2 peaks (100), (002), (101), and Bi peak (102), respectively. e) Comparison of intensity ratio of major diffraction peak of Mg_3Bi_2 (101) and Bi (102) over charge–discharge steps.

as internal standards for the analysis. The intensity of the Bi (102) peak gradually decreased during the first discharge (blue color) while the Mg₃Bi₂ peaks emerged and became dominant gradually. In the subsequent first charge process (red), the Mg₃Bi₂ peaks diminished and the Bi peaks were fully recovered. This reversible phase transformation demonstrated that Bi and Mg₃Bi₂ underwent a two-phase reaction during the electrochemical reaction.^[52] As shown in Figure 5b, the voltage profile was divided into five regions (initial state (I), first discharge (II), first charge (III), second discharge (IV), and second charge (V)), and the corresponding XRD patterns showed that the phase transitions directly corresponded to changes in the electrochemical potentials. In particular, the appearance and disappearance of Bi and Mg₃Bi₂ peaks occurred at specific voltages, indicating the stepwise formation and decomposition of the alloy phase. Figure 5c,d highlights the evolution of diffraction peaks associated with Mg₃Bi₂ and Bi within the 21°–30° range. As shown in Figure 5c, in the initial state (I), a distinct peak corresponding to metallic Bi was observed near 27° ((102) reflection), while no diffraction peaks corresponding to Mg₃Bi₂ were detected. Upon discharge (II), the metallic Bi peak disappeared gradually, and new diffraction peaks appeared around 22°, 24°, and 25° ((100), (002), (101) reflections) attributed to the formation of Mg₃Bi₂. During the subsequent first charge (III), the Mg₃Bi₂ peak disappeared and the metallic Bi peak near 27° resurfaced. This sequence was consistently observed during the second discharge (IV) and second charge (V) regions, as shown in Figure 5d, confirming the reversible alloying-dealloying reaction between Bi and Mg₃Bi₂. The

comparison of the main peak intensities of Mg₃Bi₂ (101) and Bi (102) in Figure 5e confirmed these opposite intensity trends clearly. These observations supported that the Mg ion storage mechanism in the Bi@nCN electrode is an electrochemically driven phase transition between Bi and Mg₃Bi₂ based on a reversible two-phase reaction.

2.3. Electrochemical Performance of Bi@nCN under Various Electrolytes

To demonstrate the versatility of the Bi@nCN-700 under varying electrolyte conditions, several electrolyte systems were employed to configure full cells. In contrast to previous studies that primarily focused on half-cell performance using chemically aggressive Mg alkylchloroaluminate electrolytes, the present work paired Bi@nCN anode with several MIBs cathodes to demonstrate the practical applicability in the full-cell configuration employing Cl-free electrolytes.^[26,30,45,46] Figure 6a shows the initial discharge–charge profiles associated with Mg²⁺ insertion into the Mo₆S₈ cathode^[53] from the magnesiated Bi@nCN-700 anode (Mg₃Bi₂@nCN). A constant current (64 mA g⁻¹, 0.5 C) was applied with a voltage range of 0.2–1.5 V. Mo₆S₈/Mg₃Bi₂@nCN in Cl-free electrolytes such as 0.5 M Mg(TFSI)₂ in diethylene glycol dimethyl ether (G2) or 0.5 M Mg(TFSI)₂ in acetonitrile (AN) exhibited voltage profiles comparable to those in the APC (Cl-rich) electrolyte, with similar discharge capacities (\approx 100 mAh g⁻¹) and somewhat higher overpotentials. Previous studies have shown that while many Cl-free electrolyte systems exhibited broad compatibility with diverse cathode

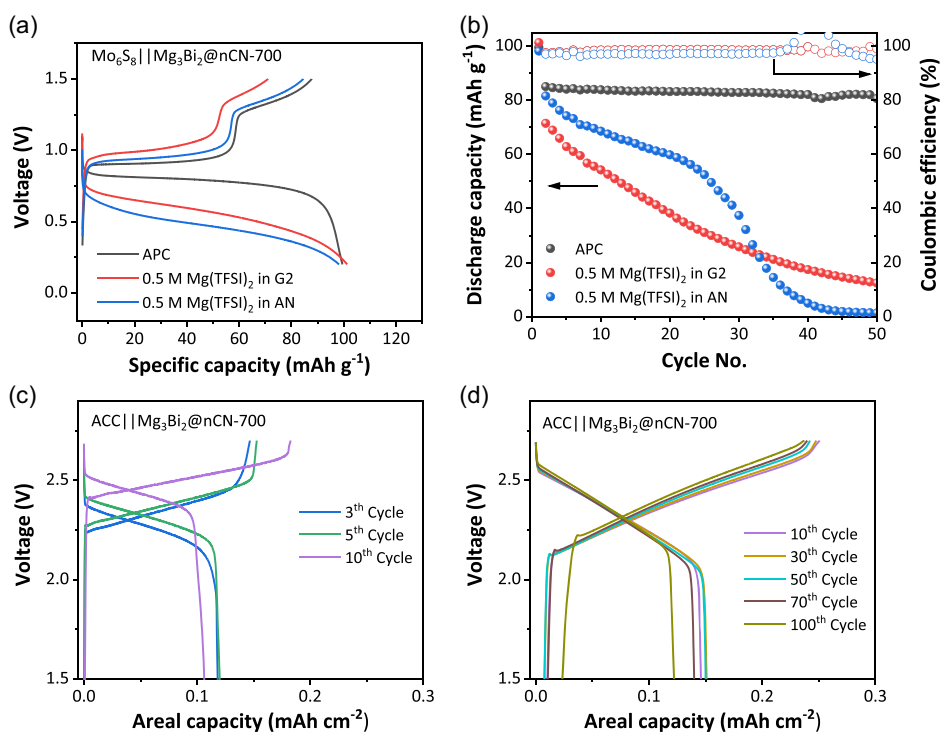


Figure 6. Electrochemical characterization of full cells with Bi@nCN anode in various cathode and electrolyte combinations. a) The voltage profiles of Mo₆S₈ with Mg₃Bi₂@nCN-700 at 0.1 C during the first cycle, and b) cycling performance up to 50 cycles in three different electrolyte systems—APC, 0.5 M Mg(TFSI)₂ in G2 and 0.5 M Mg(TFSI)₂ in AN. c,d) The voltage profiles of ACC cathode with Bi@nCN-700 anode in 0.5 M Mg(TFSI)₂ in G2 and in 0.5 M Mg(TFSI)₂ in AN, respectively, at current density of 0.1 mA cm⁻².

materials, their practical application was hindered by the formation of thick and insulating passivation layers on Mg metal anodes resulting from the electrolyte decomposition (Figure S10, Supporting Information).^[54,55] In contrast, the Bi@nCN anode successfully demonstrated distinct voltage profiles and stable cycling for decades of cycling associated with Mg-ion insertion and extraction reactions in both Cl-rich and Cl-free electrolytes (Figure 6b), suggesting that the use of Bi@nCN electrodes enables the employment of chloride-free electrolytes, thereby broadening the compatibility with a wide range of cathode materials.

As another example, the charge–discharge profiles of the full cells consisting of activated carbon cloth (ACC) cathodes and Bi@nCN-700 anodes with Cl-free electrolytes—0.5 M Mg(TFSI)₂ in G2 and 0.5 M Mg(TFSI)₂ in AN—are shown in Figure 6c,d, respectively. In these “dual-ion” cells, anions (TFSI⁻) are inserted into the graphene layers of the cathode, while Mg²⁺ ions are incorporated into the Bi anode to form Mg₃Bi₂ through an alloying process during charge and the reverse occurring during discharge. The cells were operated within a voltage range of 0.5–2.7 V at a current density of 0.1 mA cm⁻². In the case of 0.5 M Mg(TFSI)₂ in G2, stable charge–discharge profiles were obtained over ten cycles with a relatively low overpotential, indicating that anion insertion reactions occurred at the cathode, while reversible Mg₃Bi₂ alloying reactions took place at the anode. By comparison, the full-cell performance with an AN-based electrolyte, which is typically unsuitable for conventional metallic Mg anodes,^[34] is shown in Figure 6d. In this case, the cells exhibited stable cycling over 100 cycles, with capacity and voltage profiles remaining highly consistent throughout the cycling. This demonstrated the good structural and chemical stability of Bi@nCN upon repeated alloying cycling in this electrolyte. Collectively, these results highlighted the potential of Bi@nCN to overcome the limitations of conventional Mg metal anodes, offering a new opportunity to develop previously unexplored Mg-ion energy storage chemistries through broadened electrolyte and cathode selection.

3. Conclusion

In summary, finely dispersed Bi NPs embedded in nitrogen-doped carbon matrix were developed via simple CVD-like process as a practical anode material. This nanoarchitecture provided an effective buffer to accommodate volume changes during alloying–dealloying process, leading to excellent rate capability and cycling stability even at high current density, functioning in ranges of electrolyte for MIBs new way to develop advanced MIBs.

4. Experimental Section

Materials and Chemicals

Bismuth chloride (BiCl₃, ≥98%) and magnesium phthalocyanine (90%) and diethylene glycol dimethyl ether (99.5%) and acetonitrile (≥99.5%), and aluminum chloride (AlCl₃, 99.999%) were purchased from Sigma-Aldrich. Magnesium bis(trifluoromethanesulfonyl)imide

(Mg(TFSI)₂, 99.5%) was purchased from Solvionic. ACC labeled ACC-507-20 (dimensions: mass of 90 g m⁻², thickness of 0.43 mm, surface area of >1800 m² g⁻¹) was purchased from Kynol Europa GmbH. All reagents were dried in a vacuum oven for 24 h before use.

Preparation of Bi@nCN

Bi@nCN was synthesized via a straightforward thermal-treatment process involving BiOCl and magnesium phthalocyanine (Mg-Pc) precursor. For Bi@nCN preparation, a BiOCl precursor was synthesized by adding BiCl₃ to distilled water and collecting the white powder obtained by stirring for 1 h.^[56] The obtained BiOCl was dried in a drying oven at 80 °C overnight. BiOCl and magnesium phthalocyanine (Mg-Pc) were mixed at a mass ratio of 2:1 and homogeneously mixed for 30 min using a mortar mixer. The mixed precursor powder was thermally treated in a tube furnace under Ar atmosphere for 3 h to yielding the product.

Materials Characterization

TGA of respective precursors were performed (SDT Q600 V20.9) from 30 to 900 °C under N₂ atmosphere. Powder XRD patterns were obtained using an XRD (MiniFlex II, Rigaku). The surface morphology and particle size were observed using a field-emission scanning electron microscope (Regulus 8230, Hitachi) equipped with energy-dispersive X-ray spectroscopy operating at an accelerating voltage of 200 kV, and TEM (FEI Talos F200X) equipped with high-angle annular dark field-scanning transmission electron microscopy was utilized to characterize Bi@nCN. XPS (PHI 5000 Versaprobe, Ulvac-PHI) was performed, where binding energies were calibrated using the C 1s peak from adventitious carbon at 284.6 eV to compensate for the surface charging. Crystallinity of the Bi@nCN was analyzed by Raman spectra (InVia Raman Microscope, Renishaw) with a laser wavelength of 532 nm. In situ XRD during the discharge and charge processes was performed using X-ray diffractometer (Rigaku MicroMAX 007HF with R-AXIS IV++ image plate) with Mo-K_a radiation ($\lambda = 0.7107 \text{ \AA}$). For the In situ XRD analysis, Bi@nCN was cast onto a copper foil used as the working electrode, and Mg metal foil was composed of the counter electrode and APC was used as an electrolyte, and a 3 mm diameter pinhole was formed in the center of the coin cell parts for X-ray transmission. Electrical conductivity was measured by a four-point probe instrument (CMT-Series, Advanced Instrument Technology).

Electrochemical Measurements

The working electrodes were prepared by a conventional doctor-blade technique using coating slurries consisting of active materials (Bi@nCN), Super P conductor, and polyvinylidene fluoride (PVDF) binder dissolved in *N*-methyl-2-pyrrolidone (NMP) (80:10:10 wt%). Homogeneous slurries were prepared with a mini mill apparatus (Pulverisette 23, Fritsch) for 30 min, cast onto copper foil current collector, and completely dried in a vacuum oven at 80 °C. The ball-milled Bi electrode (Bi@C-BM) was prepared by a conventional doctor-blade technique using coating slurries consisting of active materials (bulk Bi), Super P conductor, and PVDF binder dissolved in NMP (52:38:10 wt%) ball-milled for 2 h with 30 min milling intervals. The resulting slurry was cast onto copper foil current collector and completely dried in a vacuum oven at 80 °C. The working electrode (mass loading of 1.5–2.0 mg cm⁻²) was assembled into coin-type cell employing a magnesium metal counter electrode and cathode, glass fiber separator, and various electrolytes. The organic electrolyte used was 0.2 M APC in THF, which was produced

according to the procedure previously reported in the literature.^[14] To prepare Mg(TFSI)₂ electrolyte with G2 and AN, 2.5 mmol of magnesium bis(trifluoromethanesulfonyl)imide powders were dissolved in G2 and AN, and solution was stirred at 80 °C for 1 h. Constant current charge–discharge experiments were performed using the multichannel battery cycler (Series 4000, MacCor Inc.) in the voltage range of 0.0–0.6 V (vs Mg/Mg²⁺) at various current rates from 0.1 to 2.0 C (1 C = 385 mA g⁻¹ for Bi@nCN). Assembly for all electrochemical cell tests was performed within an argon-filled glove box (O₂ < 0.1 ppm, H₂O < 0.1 ppm).

Acknowledgements

This work was funded by the National Research Foundation of Korea (NRF) (RS-2024-00352559), and the institutional program of Korea Institute of Science and Technology (KIST) (Project No. 2E33942) and National Research Council of Science & Technology (NST) grant by the Korea government (MSIT) (No. GTL24011-310).

Conflict of Interest

The authors declare no conflict of interest.

Data Availability Statement

The data that support the findings of this study are available from the corresponding author upon reasonable request.

Keywords: bismuth anode • bismuth magnesium alloy • electrolyte compatibility • magnesium-ion batteries • nanoarchitecture

- [1] R. Mohtadi, O. Tutusaus, T. S. Arthur, Z. Zhao-Karger, M. Fichtner, *Joule* **2021**, *5*, 581.
- [2] C. You, X. Wu, X. Yuan, Y. Chen, L. Liu, Y. Zhu, L. Fu, Y. Wu, Y.-G. Guo, T. van Ree, *J. Mater. Chem. A* **2020**, *8*, 25601.
- [3] R. Mohtadi, F. Mizuno, *Beilstein J. Nanotechnol.* **2014**, *5*, 1291.
- [4] M. Mao, T. Gao, S. Hou, C. Wang, *Chem. Soc. Rev.* **2018**, *47*, 8804.
- [5] J. Bi, J. Li, Z. Zhou, B. Li, K. Wang, G. Gao, Z. Du, W. Ai, W. Huang, *Adv. Mater.* **2025**, *37*, 2502098.
- [6] J. Zhang, Z. Chang, Z. Zhang, A. Du, S. Dong, Z. Li, G. Li, G. Cui, *ACS Nano* **2021**, *15*, 15594.
- [7] H. D. Yoo, I. Shterenberg, Y. Gofer, G. Gershinsky, N. Pour, D. Aurbach, *Energy Environ. Sci.* **2013**, *6*, 2265.
- [8] H. Kuwata, M. Matsui, N. Imanishi, *J. Electrochem. Soc.* **2017**, *164*, A3229.
- [9] J. Zhang, J. Liu, M. Wang, Z. Zhang, Z. Zhou, X. Chen, A. Du, S. Dong, Z. Li, G. Li, G. Cui, *Energy Environ. Sci.* **2023**, *16*, 1111.
- [10] D. J. Wetzel, M. A. Malone, R. T. Haasch, Y. Meng, H. Vieker, N. T. Hahn, A. Götzhäuser, J.-M. Zuo, K. R. Zavadil, A. A. Gewirth, *ACS Appl. Mater. Interfaces* **2015**, *7*, 18406.
- [11] T. Mandai, M. Watanabe, *J. Mater. Chem. A* **2023**, *11*, 9755.
- [12] Y. Li, X. Feng, G. Yang, W. Y. Lieu, L. Fu, C. Zhang, Z. Xing, M.-F. Ng, Q. Zhang, W. Liu, *Nat. Commun.* **2024**, *15*, 9364.
- [13] N. Amir, Y. Vestfrid, O. Chusid, Y. Gofer, D. Aurbach, *J. Power Sources* **2007**, *174*, 1234.
- [14] O. Mizrahi, N. Amir, E. Pollak, O. Chusid, V. Marks, H. Gottlieb, L. Larush, E. Zinigrad, D. Aurbach, *J. Electrochem. Soc.* **2007**, *155*, A103.
- [15] J. Niu, Z. Zhang, D. Aurbach, *Adv. Energy Mater.* **2020**, *10*, 2000697.
- [16] Y. Shao, M. Gu, X. Li, Z. Nie, P. Zuo, G. Li, T. Liu, J. Xiao, Y. Cheng, C. Wang, *Nano Lett.* **2014**, *14*, 255.
- [17] X. Chen, S. Wei, F. Tong, M. P. Taylor, P. Cao, *Electrochim. Acta* **2021**, *398*, 139336.
- [18] Y. Li, G. Yang, C. Zhang, W. Y. Lieu, C. Y. J. Lim, S. Sun, J. Wang, S. Jiang, Z. Xing, Z. Sofer, *Adv. Funct. Mater.* **2023**, *33*, 2210639.
- [19] Z. Zhang, M. Song, C. Si, W. Cui, Y. Wang, *eScience* **2023**, *3*, 100070.
- [20] Y.-H. Tan, W.-T. Yao, T. Zhang, T. Ma, L.-L. Lu, F. Zhou, H.-B. Yao, S.-H. Yu, *ACS Nano* **2018**, *12*, 5856.
- [21] K. V. Kravchyk, L. Piveteau, R. Caputo, M. He, N. P. Stadie, M. I. Bodnarchuk, R. T. Lechner, M. V. Kovalenko, *ACS Nano* **2018**, *12*, 8297.
- [22] J. Lee, B. Monserrat, I. Seymour, Z. Liu, S. Dutton, C. Grey **2018**.
- [23] R. Zhang, C. Ling, F. Mizuno, *Chem. Commun.* **2015**, *51*, 1487.
- [24] X. Lei, X. Liang, R. Yang, F. Zhang, C. Wang, C. S. Lee, Y. Tang, *Small* **2022**, *18*, 2200418.
- [25] C. Zhu, Y. Tang, L. Liu, X. Bai, Y. Xu, Y. Nuli, J. Wang, *Mater. Horiz.* **2023**, *10*, 1719.
- [26] K. Zheng, B. Yu, W. Ma, X. Fei, G. Cheng, M. Song, Z. Zhang, *J. Power Sources* **2024**, *613*, 234943.
- [27] S. Wei, W. Li, Z. Ma, X. Deng, Y. Li, X. Wang, *Small* **2023**, *19*, 2304265.
- [28] J. Wang, R. Yu, J. Wang, J. Long, F. Qiao, L. Zhang, G. He, Q. An, L. Mai, *J. Magnesium Alloys* **2023**, *11*, 4181.
- [29] J. Yang, Y. Liu, J. Ye, J. Wen, J. Wang, G. Huang, J. Wang, *Langmuir* **2025**, *41*, 18919.
- [30] J. Niu, H. Gao, W. Ma, F. Luo, K. Yin, Z. Peng, Z. Zhang, *Energy Storage Mater.* **2018**, *14*, 351.
- [31] D. Gu, Y. Yuan, J. Liu, D. Li, W. Zhang, L. Wu, F. Cao, J. Wang, G. Huang, F. Pan, *J. Power Sources* **2022**, *548*, 232076.
- [32] W. Jin, Z. Li, Z. Wang, Y. Q. Fu, *Mater. Chem. Phys.* **2016**, *182*, 167.
- [33] Y. Sun, Y. Wang, L. Jiang, D. Dong, W. Wang, J. Fan, Y.-C. Lu, *Energy Environ. Sci.* **2023**, *16*, 265.
- [34] T. T. Tran, W. Lamanna, M. Obrovac, *J. Electrochem. Soc.* **2012**, *159*, A2005.
- [35] Z. Xu, H. Li, M. Fu, H. Luo, H. Sun, L. Zhang, K. Li, B. Wei, J. Lu, X. Zhao, *J. Mater. Chem.* **2012**, *22*, 18230.
- [36] X. Liu, Y. Su, Q. Zhao, C. Du, Z. Liu, *Sci. Rep.* **2016**, *6*, 28689.
- [37] L. Pizarro-Castillo, A. C. Mera, G. Cabello-Guzmán, C. Bernal, M. Bizarro, C. Carrasco, M.-J. Blesa, C. A. Rodríguez, *Ceram. Int.* **2023**, *49*, 16305.
- [38] A. Patterson, *Phys. Rev.* **1939**, *56*, 978.
- [39] A. Moyseowicz, A. Moyseowicz, *Mater. Renew. Sustain. Energy* **2020**, *9*, 11.
- [40] M. Lee, Y. Yoo, J. H. Kwak, Y. S. Yun, H.-G. Jung, D. Byun, S. H. Oh, H.-D. Lim, *Chem. Eng. J.* **2021**, *412*, 128549.
- [41] K. T. Lee, X. Ji, M. Rault, L. F. Nazar, *Angew. Chem., Int. Ed.* **2009**, *48*, 5661.
- [42] E. S. Shin, M.-S. Kim, W. I. Cho, S. H. Oh, *Nanoscale Res. Lett.* **2013**, *8*, 343.
- [43] J. Jiang, Y. Zhang, Z. Li, Y. An, Q. Zhu, Y. Xu, S. Zang, H. Dou, X. Zhang, *J. Colloid Interface Sci.* **2020**, *567*, 75.
- [44] Z. Hao, X. Shi, W. Zhu, X. Zhang, Z. Yang, L. Li, Z. Hu, Q. Zhao, S. Chou, *Chem. Sci.* **2022**, *13*, 11376.
- [45] S. Pan, M. Cheng, C. Ma, H. Jing, T. Shen, J. Hu, Q. Liu, T. Wei, R. Wang, W. Li, *Chem. Eng. J.* **2025**, *505*, 159626.
- [46] M. Cheng, J. Liu, X. Wang, Y. Li, W. Xia, Q. Liu, J. Hu, T. Wei, Y. Ling, B. Liu, *Chem. Eng. J.* **2023**, *451*, 138824.
- [47] L. Zhao, X.-L. Sui, Q.-Y. Zhou, J.-Z. Li, J.-J. Zhang, G.-S. Huang, Z.-B. Wang, *J. Mater. Chem. A* **2018**, *6*, 6212.
- [48] C. Maddi, F. Bourquard, V. Barnier, J. Avila, M.-C. Asensio, T. Tite, C. Donnet, F. Garrelie, *Sci. Rep.* **2018**, *8*, 3247.
- [49] M. Lee, M. Jeong, Y. S. Nam, J. Moon, M. Lee, H.-D. Lim, D. Byun, T. Yim, S. H. Oh, *J. Power Sources* **2022**, *535*, 231471.
- [50] D. Guo, J. Qian, R. Xin, Z. Zhang, W. Jiang, G. Hu, M. Fan, *J. Colloid Interface Sci.* **2019**, *538*, 199.
- [51] M. Wassner, M. Eckardt, A. Reyer, T. Diemant, M. S. Elsaesser, R. J. Behrm, N. Hüsing, *Beilstein J. Nanotechnol.* **2020**, *11*, 1.
- [52] S. C. Jung, Y.-K. Han, *J. Phys. Chem. C* **2018**, *122*, 17643.
- [53] E. Lancry, E. Levi, A. Mitelman, S. Malovany, D. Aurbach, *J. Solid State Chem.* **2006**, *179*, 1879.
- [54] B. W. Schick, V. Vanoppen, M. Uhl, M. Kruck, S. Riedel, Z. Zhao-Karger, E. J. Berg, X. Hou, T. Jacob, *Angew. Chem., Int. Ed.* **2024**, *63*, e202413058.
- [55] A. R. Jeon, S. Jeon, G. Lim, J. Jang, W. J. No, S. H. Oh, J. Hong, S.-H. Yu, M. Lee, *ACS Nano* **2023**, *17*, 8980.
- [56] B. Yang, C. Li, H. Hu, X. Yang, Q. Li, Y. Qian, *Eur. J. Inorg. Chem.* **2003**, *2003*, 3699.

Manuscript received: August 14, 2025

Revised manuscript received: October 17, 2025

Version of record online: